J. Fluid Mech. (2008), *vol.* 597, *pp.* 343–369.
doi:10.1017/S0022112007009858 Printed in the United Kingdom

Viscous effects on wave generation by strong winds

A. ZEISEL, M. STIASSNIE, AND Y. AGNON

Department of Civil and Environmental Engineering, Technion – Israel Institute of Technology, Haifa 32000, Israel

(Received 17 April 2007 and in revised form 28 October 2007)

This paper deals with the stability of water waves in a shear flow. Both temporal and spatial growth rates are derived. A carefully designed numerical solver enables us to extend the range of previous calculations, and to obtain results for larger wavelengths (up to 20 cm) and stronger winds (up to a friction-velocity of $1\,\mathrm{m\,s^{-1}}$). The main finding is the appearance of a second unstable mode which often turns out to be the dominant one. A comparison between results from the viscous model (Orr–Sommerfeld equations) and those of the inviscid model (Rayleigh equations), for 18 cm long waves, reveals some similarity in the structure of the eigenfunctions, but a significant difference in the imaginary part of the eigenvalues (i.e. the growth rate). It is found that the growth rate for the viscous model is 10 fold larger than that of the inviscid one.

1. Introduction

1.1. *Background and motivation*

The discussion of wave generation in modern science is almost 150 years old, since the days of Kelvin, Stokes, Rayleigh and others. The history of scientific publications on the subject in the 20th century began when Jeffreys (1925) published his sheltering theory. Major progress was made with the publication of two groundbreaking studies by Miles (1957*a*) and by Phillips (1957). These two studies suggest two different mechanisms for wave generation. Phillips argued that waves can be generated by a resonance mechanism between the air turbulent eddies and the water. He assumed that the water is an inviscid fluid and the initial water state is rest. Miles proposed that the growth of waves is caused by interaction of the surface waves with a parallel shear flow. He assumed that the fluids are inviscid and presented Rayleigh's equation as the governing equation of the problem. In recent years, it has become clear that the shorter waves (with a wavelength less than say 20 cm), which contain only a small fraction of the total energy-density, play a significant role in the overall dynamics. For these waves we must include surface tension as well as viscous effects in the analysis. The growth of these shorter waves, under the influence of rather strong winds, is the focus of this paper.

1.2. *Theoretical and numerical references*

Valenzuela (1976) provides a comprehensive numerical study of the growth of gravity–capillary waves. He adopts Miles' approach and solves the coupled air–water stability problem for two viscous fluids with a shear flow. Valenzuela uses finite-difference methods in order to transform the problem into an algebraic eigenvalue problem.

Valenzuela uses the lin–log profile in both media as the base flow and shows that the shear flow in the water cannot be ignored. Kawai (1979) investigates the generation of initial wavelets, and combines experimental and theoretical studies. Kawai's main interest is in the most unstable wave which can grow under a specific friction velocity. Kawai uses a lin–log wind profile and an error-function-like current profile in his calculations. The numerical solution that Kawai uses is based on an integration of the Orr–Sommerfeld equation using a Runge–Kutta method with a filtering procedure, in order to keep the solution stable. He argues that the linear instability mechanism controls the process of wave generation from the beginning. Van Gastel, Janssen & Komen (1985) study the effect of wind on gravity–capillary waves using asymptotic methods. They too solve a pair of Orr–Sommerfeld equations. They argue that the growth rate of the initial wavelets (i.e the first waves to be generated) is proportional to u_*^3. Van Gastel *et al.* (1985) also study the effect of the wind and current profile shape, and find that the growth rate is very sensitive to the wind profile shape; the influence of the current shape is much smaller, but the drift current and the shear of the current at the interface have a significant influence on the phase velocity. Wheless & Csanady (1993) use compound matrix methods in order to integrate the Orr–Sommerfeld equation and investigate the stability of short waves. In their calculations, they use an error-function-like wind profile and an exponential current profile. They also study the effects of wind profile on the growth rate, and argue that the surface tension has a small influence; the growth rate increases when the surface tension decreases. Wheless & Csanady try to study the meaning of the eigenfunction's vertical structure and argue that the perturbation vorticity is rather high; the streamwise surface velocity perturbation in typical cases can be five times the orbital velocity of free waves on an undisturbed water surface. Hence, they suggest that unstable waves should be thought of as a fundamentally different flow structure from free waves. Boomkamp *et al.* (1997) solve the problem of waves on a thin film of liquid sheared by gas, which is a very similar problem. Boomkamp *et al.* (1997) use the Chebyshev collocation method for solving the stability problem. They introduce a robust method which converges easily for many cases and that is easy to apply. Tsai, Grass & Simons (2005) study the spatial growth of gravity-capillary waves sheared by laminar air flow, using experimental and theoretical tools. They use a fourth-order Runge–Kutta method to integrate the Orr–Sommerfeld equation and some kind of filtering scheme in order to remove parasitic errors. They use a Lock-like profile for both the wind and the current. Zhang (2005) studies the effects of shear flow on the stability of short surface waves. He uses an inviscid model, and as a result uses Rayleigh's equation as the governing equation. Zhang proposes a simplified method in order to obtain an approximate solution. The method which he calls piecewise linear approximation (PLA), approximates the wind and current profile as linear in a specific segment, and thus the curvature is zero and the equation has a very simple form. A segment of particular interest is the one that contains the critical point, where the base flow is equal to the phase velocity, and Zhang gives this segment special treatment. Stiassnie, Agnon & Janssen (2007) also study the instability of water waves where the fluids are assumed to be inviscid. They use the so-called regular approach in order to avoid the critical point when integrating Rayleigh's equation. The results of their calculation are similar to those of previous calculations for friction velocity to phase velocity ratio smaller than 2, ($u_*/c_0 < 2$); however, for friction velocity to phase velocity ratio larger than 2, they obtain a maximum in the growth rate, which does not appear in previous studies. They study both temporal and spatial growths.

1.3. *Experimental references*

Larson & Wright (1974) provide a comprehensive experimental study of the temporal growth of gravity–capillary waves. They use microwave backscatter as a measurement technique. Larson & Wright find that the growth rate is independent of the fetch, dependent on the wavenumber and varies with u_* like a power law. Caulliez, Ricci & Dupont (1998) study experimentally the first visible ripples that appear on the water surface. They argue that the laminar–turbulent transition of the near-surface water flow causes an explosive growth of the wind-generated ripples. As previously mentioned, Tsai *et al.* (2005), also perform experimental studies of the spatial growth of gravity–capillary waves. They measure a laminar wind profile at varying fetches and emphasize the development of the boundary layer with fetch. In all these papers, the subject of the wind velocity profile is a dominant issue and a variety of profiles is used.

1.4. *Wind profile studies*

Charnock (1955) measures the air mean velocity profile above a large reservoir. He finds that the air flow fits a logarithmic law. Miles (1957*b*) suggests an approximation to the solution of the boundary-layer equation which has a linear zone and a logarithmic-like profile. Many authors find this profile useful because of its smooth first derivative for all values of u_* and matching height between the linear and the logarithmic regions. Most of the field measurements were conducted at low wind speeds. As evidence of the nature of air flow above water at high-speed wind, we can cite Powell, Vickery & Rienhold (2003) who made field measurements in tropical cyclones. They found that the wind profile correlates very well with the logarithmic shape in the first 200 m.

2. Mathematical formulation

2.1. *Linear stability model*

The starting point is the governing equations for an incompressible viscous fluid flow, which are the Navier–Stokes and continuity equations.

$$\hat{\rho}\left(\frac{\partial \boldsymbol{V}}{\partial t} + \boldsymbol{V}\cdot\nabla\boldsymbol{V}\right) = -\nabla P + \mu\nabla^2\boldsymbol{V} + \boldsymbol{g}\hat{\rho}, \tag{2.1}$$

$$\nabla\cdot\boldsymbol{V} = 0. \tag{2.2}$$

We write the velocity and the pressure fields as:

$$\boldsymbol{V} = (U(z) + u(x,z,t),\ v(x,z,t)), \tag{2.3}$$

$$P = p_0 - \hat{\rho}gz + p(x,z,t). \tag{2.4}$$

Where $U(z)$ is the mean flow profile, u, v and p are harmonic perturbations of the horizontal velocity, vertical velocity, and pressure, respectively; in the above equations x and z are the horizontal and vertical coordinates, respectively, and t is the time; $g, \hat{\mu}, \hat{\rho}$ are the acceleration due to gravity, dynamic viscosity and density, respectively. We can separate the equations into harmonic terms and steady terms, and apply the assumption that the perturbations are infinitesimal, in order to linearize them. Since we are looking for a solution which has a harmonic part and a vertical dependent part, we write:

$$u = \tilde{u}(z)\mathrm{e}^{\mathrm{i}(kx-\omega t)},\quad v = \tilde{v}(z)\mathrm{e}^{\mathrm{i}(kx-\omega t)},\quad p = \tilde{p}(z)\mathrm{e}^{\mathrm{i}(kx-\omega t)},\quad \eta = \eta_0\mathrm{e}^{\mathrm{i}(kx-\omega t)}. \tag{2.5}$$

Where ω, k, η are the wave frequency, wavenumber and interface elevation, respectively. We can define a perturbation streamfunction which has the form:

$$\psi = f(z)\mathrm{e}^{\mathrm{i}(kx-\omega t)}, \tag{2.6}$$

where $f(z)$ is the auxiliary function, and the relations between the streamfunction and the velocity components give:

$$\tilde{v} = -\mathrm{i}kf(z), \quad \tilde{u} = f'(z). \tag{2.7}$$

The prime denotes vertical differentiation. After a simple elimination process, we find that the governing ODE for $f(z)$ is the Orr–Sommerfeld equation:

$$\mathrm{i}\nu(f^{(4)} - 2k^2 f'' + k^4 f) + k\left[(U-c)(f'' - k^2 f) - U'' f\right] = 0, \tag{2.8}$$

where ν and c are the kinematic viscosity and the phase velocity, respectively. The domains of the air and water are assumed to be semi-infinite, and we have boundary conditions at positive or negative infinity and at the interface between the fluids. At infinity, the perturbations are assumed to decay exponentially. At the interface, we impose the kinematic boundary condition, horizontal velocity continuity, shear stress continuity and the dynamic boundary condition (continuity of normal stress). All of the boundary conditions are imposed at $z=0$, after the linearization procedure. For the full formulation of the boundary conditions see Valenzuela (1976). We choose the reference problem of linear water waves without wind and current, neglecting the influence of the air, for which the wavenumber and the wave frequency are related by:

$$\omega_0^2 = gk_0 + \frac{\sigma k_0^3}{\rho_w}, \tag{2.9}$$

where σ is the surface tension. Transforming to dimensionless quantities (note that the circumflex in (2.10) denotes a dimensional quantity):

$$\begin{gathered} \omega = \frac{\hat{\omega}}{\omega_0}, \quad k = \frac{\hat{k}}{k_0}, \quad c = \frac{\hat{c}}{c_0}, \\ z = \hat{z}k_0, \quad U = \frac{\hat{U}}{c_0}, \quad f = \frac{\hat{f}k_0}{\eta_0\omega_0}. \end{gathered} \tag{2.10}$$

Defining the dimensionless numbers of the problem:

$$R_{w,a} = \frac{c_0}{\nu_{w,a}k_0}, \quad F = \frac{1}{F_r^2} = \frac{gk_0}{\omega_0^2}, \quad W = \frac{1}{W_e} = \frac{\sigma k_0^3}{\rho_w\omega_0^2}, \quad \rho = \frac{\rho_a}{\rho_w}, \quad \mu = \frac{\mu_a}{\mu_w}, \tag{2.11}$$

where R is the Reynolds number, F is the inverse square Froude number, W is the inverse Weber number, ρ is the density ratio and μ is the dynamic viscosity ratio. The subscripts w and a refer to water and air, respectively. The complete eigenvalue problem must satisfy the following system:
Two ODEs:

$$\underbrace{\mathrm{i}R_w^{-1}\left(f_w^{(4)} - 2k^2 f_w'' + k^4 f_w\right)}_{\text{Viscous terms}} + k\left[(U_w - c)\left(f_w'' - k^2 f_w\right) - U_w'' f_w\right] = 0, \quad z \in (-\infty, 0], \tag{2.12}$$

$$\underbrace{\mathrm{i}R_a^{-1}\left(f_a^{(4)} - 2k^2 f_a'' + k^4 f_a\right)}_{\text{Viscous terms}} + k\left[(U_a - c)\left(f_a'' - k^2 f_a\right) - U_a'' f_a\right] = 0, \quad z \in [0, \infty). \tag{2.13}$$

Nine boundary conditions:

$$f_a(0) = c - U(0), \qquad f_w(0) = c - U(0), \tag{2.14}$$

$$f_w' + U_w' = f_a' + U_a' \qquad \text{at } z = 0, \tag{2.15}$$

$$\mu(f_a'' + k^2 f_a + U_a'') = (f_w'' + k^2 f_w + U_w'') \qquad \text{at } z = 0, \tag{2.16}$$

$$kf_w'(c - U_0) + kf_w U_w' + \underbrace{\mathrm{i}R_w^{-1}\left(3k^2 f_w' - f_w'''\right)}_{\text{Viscous terms}} - kF$$

$$= \rho\left[kf_a'(c - U_0) + kf_a U_a' + \underbrace{\mathrm{i}R_a^{-1}\left(3k^2 f_a' - f_a'''\right)}_{\text{Viscous terms}} - kF\right] + Wk^3 \text{ at } z = 0, \tag{2.17}$$

$$f_w(z) \to 0, \qquad f_w'(z) \to 0, \qquad z \to -\infty, \tag{2.18}$$

$$f_a(z) \to 0, \qquad f_a'(z) \to 0, \qquad z \to \infty. \tag{2.19}$$

When formulating the inviscid model, we neglect the viscous terms in (2.12) and (2.13) and obtain two Rayleigh equations. The boundary conditions will be the kinematic boundary condition in the same form (2.14), and the dynamic boundary condition without the viscous terms (2.17). Conditions (2.15) and (2.16) do not apply when formulating the inviscid case. Both the viscous and inviscid models are classified as eigenvalue problems. The calculations will focus on the temporal and spatial cases, meaning that the growth can be only either in space, or in time. For the temporal case we specify k and search for ω, and for the spatial case we specify ω and search for k.

2.2. *Mean flow profile*

In (2.12) to (2.19), $U(z)$ represents the mean flow profile. It is already well known (Kawai 1979; Van Gastel *et al.* 1985; Wheless & Csanady 1993), that the results are sensitive to the profile shape. The exact mean flow profile above water waves is still uncertain. Miles (1957*b*) suggests a profile which fits well the mean flow profile above a flat plate. This profile was used in previous studies Valenzuela 1976; Kawai 1979; Van Gastel *et al.* 1985), and was named the 'lin–log' profile. We use this profile for the air, and an exponential profile for the current in the water.

In the air (wind profile):

$$U_a = \begin{cases} U_0 + \dfrac{u_*^2}{\nu_a} z, & z \leqslant z_1, \\ U_0 + mu_* + \dfrac{u_*}{\kappa}\left[\alpha - \tanh\left(\dfrac{\alpha}{2}\right)\right], & z \geqslant z_1, \end{cases} \tag{2.20}$$

and in the water (current profile):

$$U_w = U_0 \exp\left(\frac{\rho_a u_*^2}{U_0 \mu_w} z\right) \tag{2.21}$$

where,

$$\alpha = \sinh^{-1}(\beta), \quad \beta = \frac{2\kappa u_*}{\nu_a}(z - z_1), \quad z_1 = \frac{m\nu_a}{u_*}, \quad U_0 = Bu_*, \quad m = 5, \quad B = 0.5, \tag{2.22}$$

where u_* is the friction velocity. The wind profile has a linear segment with a possible offset (drift current) and a segment that is asymptotically logarithmic. The parameter

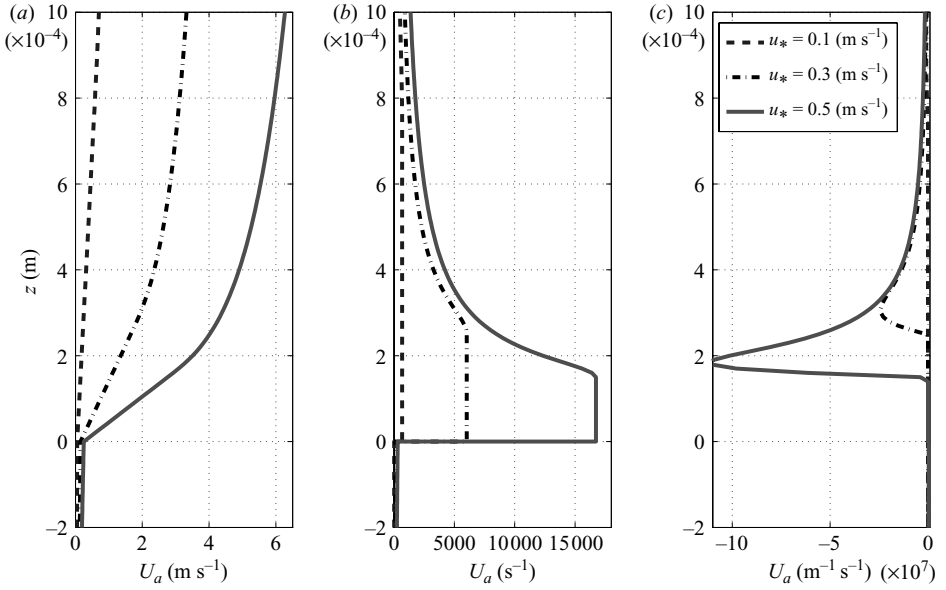

FIGURE 1. The base flow and its first two derivatives for the linear–logarithmic profile and various values of u_* ($m = 5$). (*a*) The velocity profile, (*b*) the first derivative, (*c*) the second derivative.

m in (2.22) defines the thickness of the viscous sublayer (the linear segment), and thus influences the derivative at the interface. This profile enables continuity of the function and its first two derivatives at the matching point $z = z_1$ for all values of the parameters m and U_0. The value of m is set to 5 (usually $m = 5-8$), whereas the value of B is chosen to be $B = 0.5$ according to Kawai (1979), this value can sometimes be taken as $B = 0.3$ as found by Zhang & Harrison (2004), but qualitatively it would not change the results. The value of B controls the drift current, but also influences the derivatives of the current. This profile, in (2.20) and (2.21), maintains the continuity of the shear stress between the air and the water, $\mu_a U_a' = \mu_w U_w'$.

As can be seen in figure 1, the friction velocity u_* defines the wind intensity as well as the current profile. The first and second derivatives have discontinuities at the interface, but are continuous in the air. The first two derivatives have increasing absolute values as u_* increases.

2.3. *Alternative wind profile*

As an alternative wind profile, we present a wind profile which will enable us to compare the inviscid and viscous solutions under strong winds. This profile is based on the numerical solution of the turbulent boundary-layer equation, which is:

$$\underbrace{\mu_a \frac{\mathrm{d}U}{\mathrm{d}z}}_{\text{Laminar stress}} + \underbrace{\rho_a \kappa^2 z^2 \left(\frac{\mathrm{d}U}{\mathrm{d}z}\right)^2}_{\text{Turbulent stress}} = \tau_0 = \rho_a u_*^2. \tag{2.23}$$

The equation is based on Prandtl's mixing-length theory. The numerical solution produces a profile which is very similar to the lin–log profile, but with a much thinner viscous sublayer. This profile has zero curvature only at $z = 0$. The current (water flow) used is exactly the same as in (2.21). Note that the parameter m is not needed, and the parameter $B = 0.5$. The meanings of the other parameters are the same as in

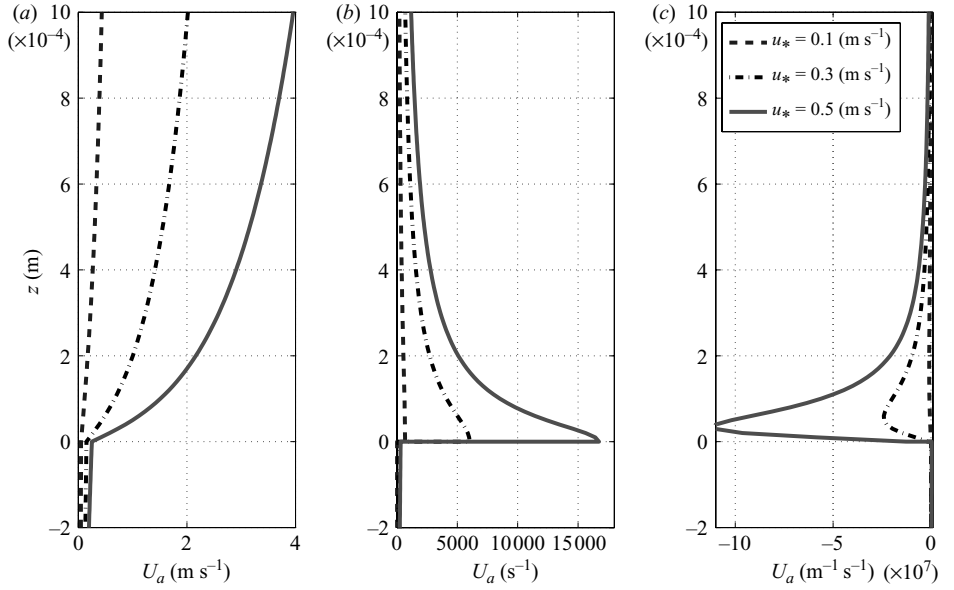

FIGURE 2. The base flow and its first two derivatives from the numerical integration of the boundary-layer equation for various values of u_*. (*a*) The velocity profile, (*b*) the first derivative, (*c*) the second derivative.

§ 2.2. The benefit from this kind of profile is that it enables to compare the viscous and inviscid solutions at any wind intensity. We named this profile the 'numerical' profile. The profile and its derivatives are described in figure 2; it is very similar to the lin–log profile, but with a much thinner viscous sublayer.

3. Numerical procedure and its validation

3.1. *Numerical procedure*

The numerical procedure which we used to solve the eigenvalue problem of the viscous model is based on the Chebyshev collocation method. We chose this method because of the difficulties in the integration of the Orr–Sommerfeld equation, which forced some of the previous authors to use filters in order to remove parasitic errors. Another reason for this choice is the nature of the Chebyshev grid which is characterized by a high density of grid points near the boundaries. The Chebyshev grid is:

$$x_j = \cos\left(\frac{j\pi}{N}\right) \ \forall j = 0, 1, \ldots, N. \tag{3.1}$$

The method approximates an unknown function by a finite series of Chebyshev polynomials see (Trefethen 2000).

$$\phi(x) = \sum_{n=0}^{N} a_n T_n(x). \tag{3.2}$$

Chebyshev expansions are done in the interval $[-1, 1]$, where the Chebyshev polynomials are orthogonal. In the numerical solution, the computational domain was divided into three finite subintervals. This subdivision is similar to that of Boomkamp *et al.* (1997). The size of the finite interval is set to be $z_\infty = 10$, which

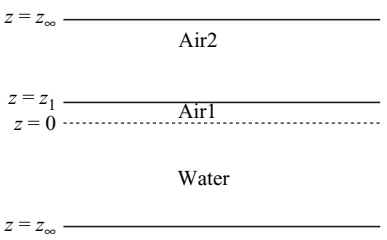

FIGURE 3. Computational domain of the problem.

means that $z_{dimensional,\pm\infty} \approx \pm 1.6\lambda$, where $\lambda = 2\pi/k_0$ is the reference wavelength. The lower interval is for the water, the upper layer (air2) is for the logarithmic air region, and the intermediate interval (air1) is for the viscous sublayer region (see figure 3). Linear transformations are used to transform each interval into $[-1, 1]$, which is where the Chebyshev polynomials are orthogonal.

Since the problem at hand is an eigenvalue problem, we search for a pair ω, k which causes the solution to obey all 9 boundary conditions. An iterative process to find this eigenvalue was built. This process begins with an initial guess for the eigenvalue; the next stage is to solve the coupled BVP (boundary value problem) and finally to use a standard secant method to produce an improved guess. The process is stopped when a convergence condition, requiring four significant digits in the imaginary part of the eigenvalue, is satisfied. The Chebyshev collocation method is used for the solution of the BVP. This search process provides only one eigenvalue at a time; the specific eigenvalue which the process converges to depends on the initial guess. This approach is different from the one of solving the generalized eigenvalue problem and finding all of the eigenvalues, see Boomkamp *et al.* (1997).

In practice, we reduce the order of the Orr–Sommerfeld equation by defining $V \triangleq f''$ and replacing the Orr–Sommerfeld equation with the system:

$$V - f'' = 0, \tag{3.3a}$$

$$iR^{-1}(V'' - 2k^2V + k^4 f_a) + k\left[(U_a - c)(V - k^2 f_a) - U_a'' f_a\right] = 0. \tag{3.3b}$$

The next step is to transform the differential equations into an algebraic form with the help of the Chebyshev differentiation matrices. We solved the BVP with all of the boundary conditions, except for the dynamic boundary condition (2.17). In practice we, add an artificial interface between the air1 domain and the air2 domain, and actually solve three coupled Orr–Sommerfeld equations. The boundary conditions between air1 and air2 are similar to the boundary conditions between the water and air in their physical meaning; but since the density, viscosity and the base flow are continuous, they are written as:

$$f_{a2}(z_1) = f_{a1}(z_1), \quad f'_{a2}(z_1) = f'_{a1}(z_1), \quad f''_{a2}(z_1) = f''_{a1}(z_1), \quad f'''_{a2}(z_1) = f'''_{a1}(z_1). \tag{3.4}$$

The iterative process is built for the function $G(\omega, k)$, which is defined as:

$$G(k, \omega) = kf'_w(c - U_0) + kf_w U'_w + iR_w^{-1}(3k^2 f'_w - f'''_w) - kF$$
$$- \rho\left[kf'_a(c - U_0) + kf_a U'_a + iR_a^{-1}(3k^2 f'_a - f'''_a) - kF\right] - Wk^3 \text{ at } z = 0. \tag{3.5}$$

$G = 0$ is the dynamic boundary condition, see (2.17). Using the function G, we can define the dynamic boundary condition plot. A dynamic boundary condition plot is a plot of the isolines of $\|G\|^2$ in the complex ω (or k) plane. The function G is a

$u* = 0.3\text{m s}^{-1}$, $\lambda = 0.01\text{m}$ temporal case lin log wind profile exponential current

N_{a1}	$M = 2.2$	$M = 1$
30	1.35384 + 0.017398i	1.35748 + 0.014870i
50	1.35360 + 0.017512i	1.35344 + 0.017645i
70	1.35360 + 0.017512i	1.35358 + 0.017526i
90	1.35360 + 0.017512i	1.35360 + 0.017509i
110	1.35360 + 0.017512i	1.35360 + 0.017512i
130	1.35360 + 0.017512i	1.35360 + 0.017512i

$u_{al} = 1\text{m s}^{-1}$, $\lambda = 0.2\text{m}$ temporal case lin log–wind profile exponential current

N_{a1}	$M = 2.2$	$M = 1.5$
120	0.79809 + 0.59893*i*	2.20140 + 0.12182i
140	0.51149 + 1.01276*i*	1.74337 + 0.22800i
160	0.48421 + 1.12226*i*	1.19489 + 0.39902i
180	0.48430 + 1.12786*i*	0.71359 + 0.66407i
200	0.48834 + 1.11202*i*	0.52574 + 0.96493i
220	0.49267 + 1.09481*i*	0.49011 + 1.09063i
240	0.49585 + 1.08125*i*	0.48329 + 1.12708i
260	0.49821 + 1.07237*i*	0.48389 + 1.12925i

TABLE 1. Convergence of the Chebyshev collocation method for two wind intensities and wavelengths, temporal case. Where $N_{a1} = N_w$, $N_{a2} = MN_{a1}$. (Values of ω.)

property of the BVP, and, to a certain extent, it defines the distance between a chosen solution of the BVP and that of the eigenvalue problem. Note that all the results in this paper were calculated using the following numerical values:

$$\left.\begin{aligned} \kappa = 0.41,\ \mu_w = 10^{-3}\text{pa s},\ \mu_a = 1.83\,10^{-5}\text{pa s},\\ \rho_a = 1.225\text{kgm}^{-3},\ \rho_w = 1000\text{kg m}^{-3},\ g = 9.81\text{ms}^{-2},\ \sigma = 0.075\text{N m}^{-1} \end{aligned}\right\} \tag{3.6}$$

3.2. *Validation of the numerical results*

In this section we will show the convergence of the Chebyshev collocation method, test the sensitivity of the model to the interval size and compare the results with a test case and previous studies. An analytical solution for the viscous problem with a linear wind profile and a constant current is given in the Appendix, and serves as the test case.

3.2.1. *Convergence of the Chebyshev collocation method*

As mentioned above, the computational domain is divided into three sub intervals: the water $[-z_\infty, 0]$, the air1 $[0, z_1]$ and the air2 interval $[z_1, z_\infty]$. In each of these intervals we can control the number of collocation points (the grid). If the method converges, the change in the results should be minor when changing the number of collocation points. From numerical experiments, we learn that the interval air1 is the most important interval and therefore requires a high resolution grid. We show convergence, for the case where the number of collocation points in the interval air1 N_{a1} is equal to those in the water N_w, and the number of collocation points in air2 will be $N_{a2} = MN_{a1}$, where M is a parameter (see table 1). As we can see from the data in the table, the process converges up to at least two significant digits. Of course, the case of longer wavelength and high wind intensities required more grid points. Note that differences between $M = 1, 1.5$ to $M = 2.2$ are of the order of 1%.

	$u_* = 0.3\,\mathrm{m\,s^{-1}}$ $\lambda = 0.01\,\mathrm{m}$	$u_* = 0.8\,\mathrm{m\,s^{-1}}$ $\lambda = 0.01\,\mathrm{m}$
$z_\infty = 5$	$1.35357 + 0.017523\mathrm{i}$	$1.55164 + 0.22261\mathrm{i}$
$z_\infty = 10$	$1.35360 + 0.017512\mathrm{i}$	$1.55166 + 0.22260\mathrm{i}$
$z_\infty = 15$	$1.35360 + 0.017512\mathrm{i}$	$1.55166 + 0.22260\mathrm{i}$
$z_\infty = 20$	$1.35360 + 0.017512\mathrm{i}$	$1.55166 + 0.22260\mathrm{i}$

TABLE 2. The sensitivity of ω to different z_∞, temporal case, lin–log wind profile, exponential current.

		Temporal case		
		$\lambda = 0.001\mathrm{m}$	$\lambda = 0.1\mathrm{m}$	$\lambda = 0.2\mathrm{m}$
$u_* = 0.001\,\mathrm{m\,s^{-1}}$	Numerical	$1.0705 - 0.017431\mathrm{i}$	$1.1246 + 0.0071116\mathrm{i}$	$1.0908 + 0.0091061\mathrm{i}$
	Analytical	$1.0705 - 0.017431\mathrm{i}$	$1.1246 + 0.0071115\mathrm{i}$	$1.0908 + 0.0091070\mathrm{i}$
$u_* = 0.005\,\mathrm{m\,s^{-1}}$	Numerical	$1.3628 - 0.016102\mathrm{i}$	$1.7260 + 2.2254\mathrm{i}$	$1.7684 + 2.5485\mathrm{i}$
	Analytical	$1.3628 - 0.016102\mathrm{i}$	$1.7262 + 2.2254\mathrm{i}$	$1.7680 + 2.5489\mathrm{i}$
$u_* = 1\,\mathrm{m\,s^{-1}}$	Numerical	$1.7132 - 0.000028672\mathrm{i}$	$0.47194 - 7.6548\mathrm{i}$	$5.3226 + 8.4767\mathrm{i}$
	Analytical	$1.7132 - 0.000029147\mathrm{i}$	$0.46973 - 7.6153\mathrm{i}$	$5.3219 + 8.4752\mathrm{i}$

TABLE 3. Comparison with test case, temporal case for various wind intensities and wavelength. (Values of ω.)

3.2.2. *Sensitivity to* z_∞

Since, in practice, we need to use a finite interval for the numerical calculations, we must show that our choice does not have a major effect on the results. The z coordinate is normalized by k_0 in the form $z = z_{dimensional} k_0$. From a physical aspect, the value of z_∞ should be related to the wavelength. From linear theory of water waves, it is known that at depths below half a wavelength, the influence of the waves on the flow field is minor. The value which we use for most of our calculations is $z_\infty = 10$, which means that $z_{\infty,dimensional} = 10\lambda/(2\pi) = 1.591\lambda$. In order to justify this value, we made a few runs with different values of z_∞. Note that in this method, when we change the interval size we need to change the number of collocation points in order to keep a fine grid in the critical region. From table 2 we can state that if there is an error it is in the fourth digit.

3.2.3. *Comparison with the test case*

In order to validate the numerical results, we want to compare them with an analytical solution. The case which we compare them with is the one mentioned at the beginning of § 3.2. The analytical solution of this case is based on a combination of Airy and exponential functions, thus the numerical solution is not so trivial, for details see Appendix. Such a comparison has significant meaning, because the methods which were used to obtain the results are completely different from each other. The comparison was made for the spatial case, as well as for the temporal case. The current was constant with the value of $U_w = 0.5u_*$ and the velocity slope of the wind was u_*/ν_a. These conditions are similar to those which were used in the lin-log profile. The results are described in table 3. The maximum error in this comparison is 2%, whereas in most of the cases the error is smaller than 1%.

3.2.4. *Comparison with previous studies*

The last stage in the validation process will be a comparison with previous calculations of Kawai (1979), Van Gastel *et al.* (1985) and Tsai & Lin (2004).

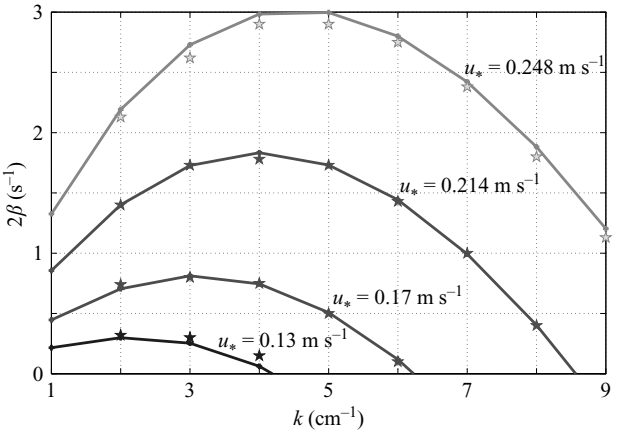

FIGURE 4. Energy growth rate *vs.* wavenumber, temporal case. Comparison with previous studies. Solid line, our study; five point star, results from Tsai & Lin (2004), (analogous to figure 2 in Tsai & Lin 2004).

They all compute similar values for the temporal growth rate, but for a rather small domain in the (λ, u_*)-plane. Figure 4 is analogous to figure 2 in Tsai & Lin (2004).

In figure 4, there are symbols of our calculations and symbols of Tsai & Lin's calculations taken from figure 2 in Tsai & Lin (2004). We can see that the results of Tsai & Lin (2004) are similar to our results; the difference is up to 5%, but is typically of the order of 1%. For the spatial case, we are not familiar with previous studies to which it may be compared. Finally, it seems safe to say that for the range of $\lambda \in (0.001, 0.2)$ m, $u_* \in (0, 1)$ m s^{-1}, our numerical results are reliable. In most cases, accuracy is to the first four digits, whereas in the more difficult cases it is only to the first two significant digits.

4. A second eigenvalue at high wind intensities

4.1. *Results for the temporal case*

A number of studies concerning the surface wave stability problem have been conducted (e.g. Valenzuela 1976; Tsai *et al.* 2005 and references therein). All of the results that we found were limited in wind intensity and in wavelength/wave period. Most of the theoretical studies focus on the temporal case, except for Tsai *et al.* (2005) which deals with spatial evolution for a laminar base flow. The domain of previous calculations in the range of approximately, wavelength $0 < \lambda < 7$ cm, and friction velocities $0 < u_* < 0.5$ m s^{-1}, is plotted in figure 5. As described in § 3.2, our solver for the viscous problem is valid in the domain $0 < \lambda < 20cm, 0 < u_* < 1m/sec$ (the entire region of figure 5). The calculations were done using several types of profiles for the temporal case as well as for the spatial case. From previous studies, we learn that for each scenario there can be only one unstable mode. This unstable mode was calculated by several authors and has been confirmed by our calculations (see figure 4). Since the problem is an eigenvalue problem, it is reasonable to search for more eigenvalues. However, we are dealing with a physical problem, and the physical meaning is also important. When we began to expand the domain of calculations, we discovered the presence of a second unstable mode. In certain cases, this can mean that for a given wavelength and wind intensity, there are two kinds of unstable waves with different growth rates and different phase velocities. As described in figure 5, the

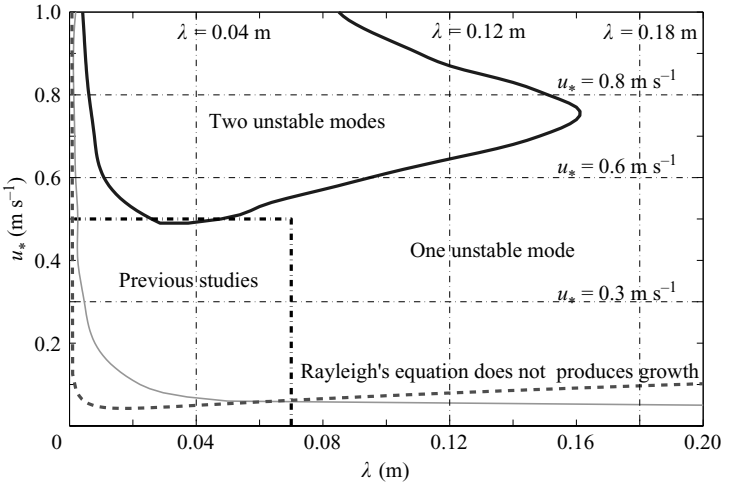

FIGURE 5. Instability domains of the solution over the (λ, u_*)-plane. solid line, boundary of the region where there are two unstable modes; solid thin line- neutral line (zero growth rate); dash-dot line, the domain of previous studies; dashed line, the region where the inviscid model produces growth. Temporal case, the profile is according to (2.20)–(2.22).

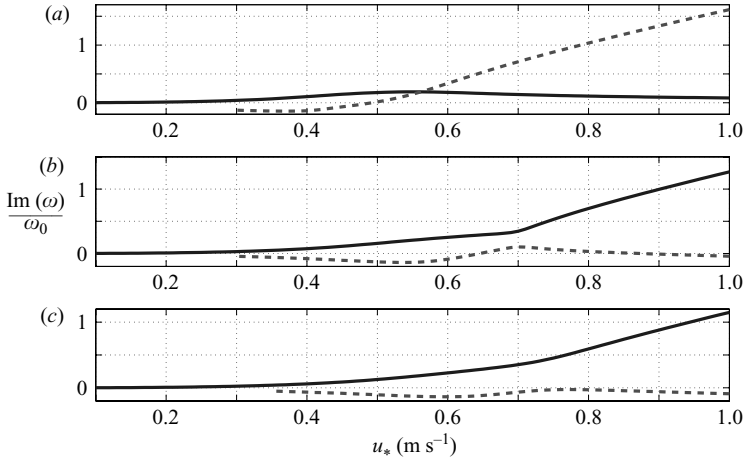

FIGURE 6. Normalized imaginary part of the frequency *vs.* friction velocity for various wavelengths, two modes are shown in the region of interest, temporal case, the profile is according to (2.20)–(2.22). (*a*) $\lambda = 0.04$ m, (*b*) $\lambda = 0.12$ m, (*c*) $\lambda = 0.18$ m. The solid line and the dashed line are two distinct solutions for the specific scenario.

plane (λ, u_*) can be divided into three different regions. The first region is the region without growth, in this region the growth due to the wind is smaller than the decay due to viscosity. The second region is the region with one unstable mode, and the third region is the one with two unstable modes. The calculations were done along cross-sections of the (λ, u_*)-plane, where λ or u_* remain constant. For example, we start with one solution at $u_* = 1\,\mathrm{m\,s^{-1}}$ and try to progress along the same branch of the solution by slowly decreasing the friction velocity. In figures 6 and 7 we present typical cross-sections. For a short wave $\lambda \sim 4$ cm, a typical cross-section shows that at low wind intensities there is only one unstable mode, while at $u_* \sim 0.5\,\mathrm{m\,s^{-1}}$ another

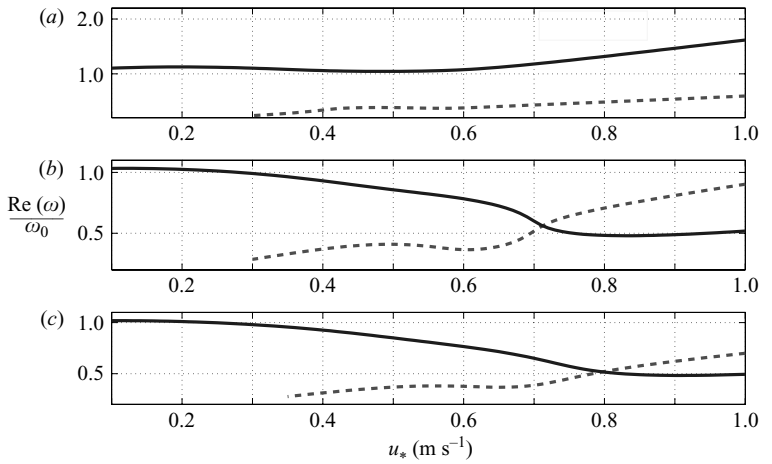

FIGURE 7. Normalized real part of the frequency vs. friction velocity for various wavelengths, two modes are shown in the region of interest, temporal case, the profile is according to (2.20)–(2.22). (*a*) $\lambda = 0.04$ m, (*b*) $\lambda = 0.12$ m, (*c*) $\lambda = 0.18$ m. The solid line and the dashed line are two distinct solutions for the specific scenario.

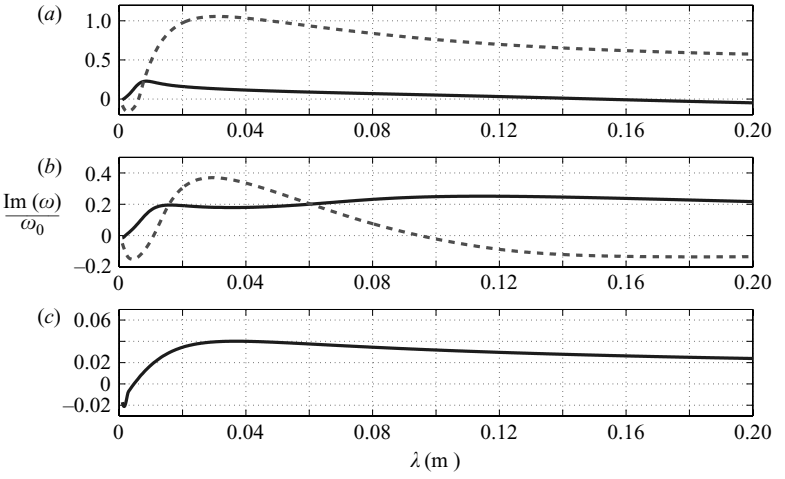

FIGURE 8. Normalized imaginary part of the frequency vs. wavelength for various friction velocities, two modes are shown in the region of interest, temporal case, the profile is according to (2.20)–(2.22). (*a*) $u_* = 0.8$ m s^{-1}, (*b*) $u_* = 0.6$ m s^{-1}, (*c*) $u_* = 0.3$ m s^{-1}. The solid line and the dashed line are two distinct solutions for the specific scenario.

mode becomes unstable. We can see that the lines cross each other in the imaginary part, but in the real part these two lines never intersect. At longer wavelengths, the line of the second unstable mode passes the zero growth level at a stronger wind, and then turns back and becomes stable; at even longer wavelengths the second mode is always stable. When looking at the real part of the same results, figure 7, we can see that, for the short waves, the lines of the separate modes never cross each other, while in longer waves the lines intersect. The meaning of these intersection points is that there are two waves with the same wavelength and wave frequency, but with different growth rates. When looking at the cross-sections along λ (see figures 8 and 9), we

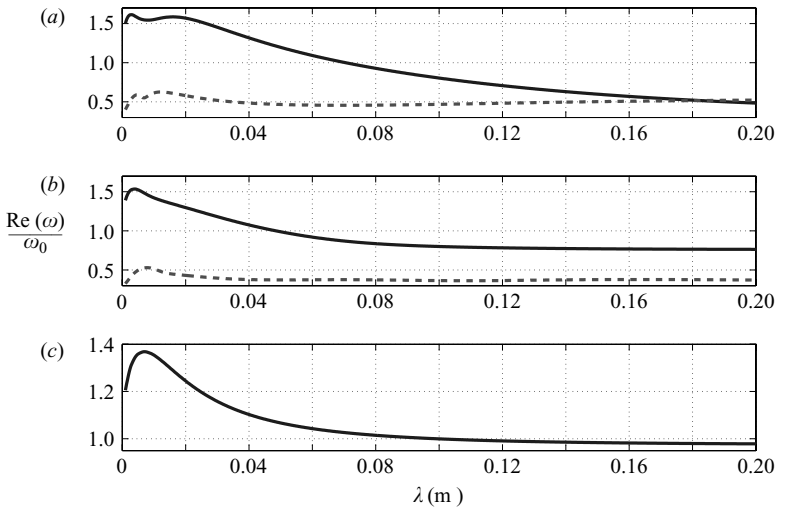

FIGURE 9. Normalized real part of the frequency *vs.* wavelength for various friction velocities, two modes are shown in the region of interest, profile is according to (2.20)–(2.22). (*a*) $u_* = 0.8\,\mathrm{m\,s^{-1}}$, (*b*) $u_* = 0.6\,\mathrm{m\,s^{-1}}$, (*c*) $u_* = 0.3\,\mathrm{m\,s^{-1}}$. The solid line and the dashed line are two distinct solutions for the specific scenario.

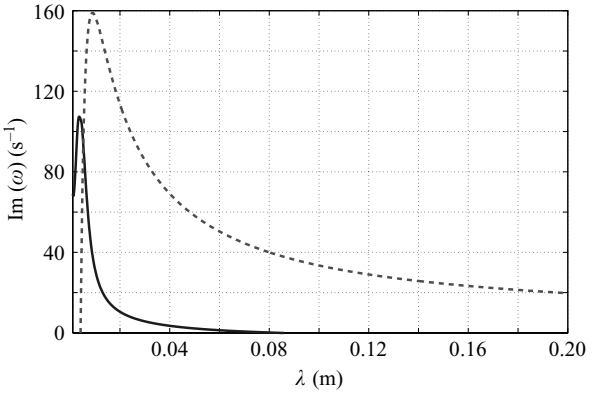

FIGURE 10. Temporal growth rate *vs.* wavelength, $u_* = 1\,\mathrm{m\,s^{-1}}$, the profile is according to (2.20)–(2.22). The solid line and the dashed line are two distinct solutions for the specific scenario.

can distinguish a few characteristics of the solution. First, at low wind intensities, there is only one unstable mode for every wavelength, while at stronger winds, above a critical value, there are two unstable modes in a range of wavelengths. For example, see the lines of $u_* = 0.6\,\mathrm{m\,s^{-1}}$, $0.8\,\mathrm{m\,s^{-1}}$ in figure 8. All of the lines in the figure of the imaginary part are characterized by one maximum point. These maximum points describe the most unstable wave, but since figure 8 presents the normalized quantity it is simpler to look at the dimensional figure (see figure 10). When there are two lines, it is typical that the maximum point of the second unstable mode occurs at a longer wavelength. Another point that may be of some interest is the point of zero growth (neutral point) on the left-hand side, which indicates the shortest wave that can be generated. In this aspect, again, the lines of the second unstable mode start to

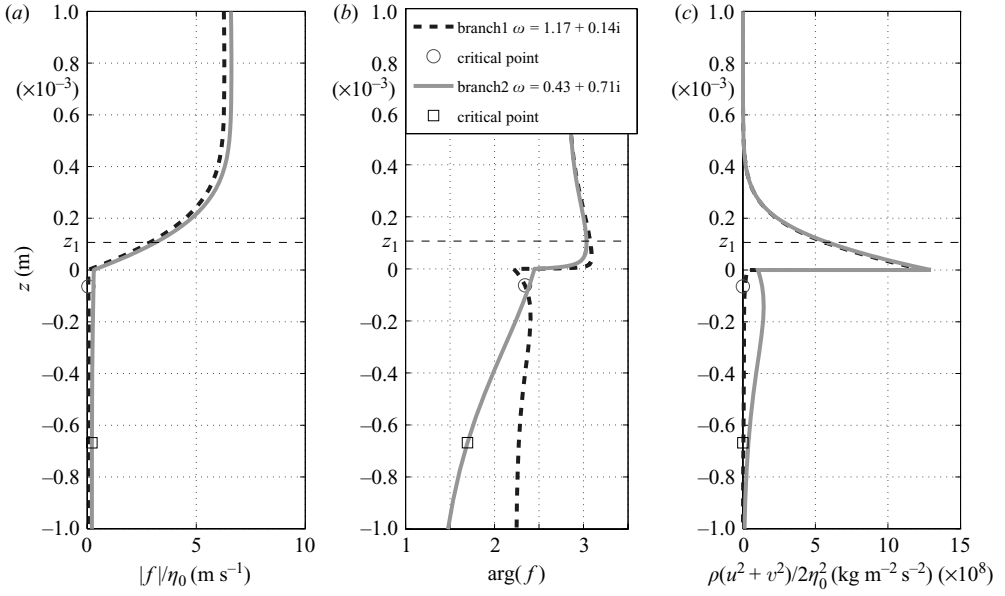

FIGURE 11. Comparison of the vertical structure of the eigenfunction and the kinetic energy density between the two modes for $\lambda = 0.04$ m, $u_* = 0.7$ m s^{-1}, temporal case, profile is according to (2.20)–(2.22). (*a*) absolute value of the eigenfunction, (*b*) argument of the eigenfunction, (*c*) kinetic energy density.

produce growth for longer wavelengths. The results for both, the point of maximum growth and the neutral point, are very intuitive and show that: when increasing the wind intensity, the value of maximum growth becomes larger and the wavelengths of maximum growth and zero growth become shorter. The real part of the eigenvalue, described in figure 9, shows a major difference between these two branches of the solution. While one of the branches has a phase velocity which is often higher than the reference case, ($\mathrm{Re}(\omega)/\omega_0 > 1$), the second branch has a phase velocity which is lower than the reference case, ($\mathrm{Re}(\omega)/\omega_0 < 1$). The result that the phase velocity of the wave usually decreases when the friction velocity increases is not very intuitive. This result was also obtained by Valenzuela (1976).

In figure 10 the temporal growth rate is presented in dimensional form. As we can see, the values of the growth rate are very large, especially for waves in the gravity–capillary range. These 'explosive' growth rates which can exist in very strong winds ($u_* = 1$ m s^{-1}, i.e. $U_{10} = 37$ m s^{-1}), indicate that these ripples attain their maximum steepness almost immediately, and break continuously.

While comparing the eigenfunctions of both modes in figure 11, we can see a significant similarity in the air region, but a profound difference in the water region. The horizontal dashed line in this figure indicates the edge of the laminar layer, and it is clear that most of the energy transfer from the mean flow to the disturbance happens within this layer. The square and circle symbols indicate the location of the so-called critical point, where the mean flow velocity is equal to the actual phase velocity. We can see that the critical-points, for both modes, are in the water and that they do not play any significant role in the case at hand.

After finding the second unstable mode, we try to characterize the conditions for the existence of this mode. We cannot formulate a complete condition yet, but we

can state that the second unstable mode appears only when the mean flow profile includes a shear current. Another condition is that the wind intensity will be above a critical value. The results in the figures were calculated for a specific lin–log profile ($m = 5$, $B = 0.5$ see (2.22)), the parameter B which controls the drift current has a major influence on the critical conditions for the appearance of the second mode. In order to identify the conditions that influence the appearance of the second unstable mode, we have tried many combinations of wind profiles/intensities and current profile/intensities. In figure 12, we present six dynamic boundary condition plots, (see definition in § 3.1) that demonstrate the behaviour of the problem for different scenarios. The left-hand column is for a relatively low wind intensity ($u_* = 0.3\,\mathrm{m\,s^{-1}}$), and the right-hand column is for a high wind intensity ($u_* = 0.8\,\mathrm{m\,s^{-1}}$), whereas the three different rows are for current only (no wind), wind with constant current (no shear in the water), and wind with exponential current; from top to bottom, respectively. From figures 12(*a*) and 12(*d*), we can see that the exponential current by itself can cause instability, but does not cause two unstable modes. From figures 12(*b*) and 12(*e*), we can conclude that a current without shear can not cause two unstable modes. In figures 12(*c*) and 12(*f*), we can see that for the combination of the wind and current the picture looks very different, particularly at strong winds, where the two unstable modes appear.

As already mentioned, the physical reason for the appearance of the second growing eigenvalue is not entirely clear. However, the fact that its phase velocity is smaller than c_0 (sometimes much smaller), and that it appears only above a threshold of u_*, which corresponds to a threshold in the drift-current, provides some indication that the second eigenvalue originates from a left moving wave which evolved into a right moving wave under the influence of the current. To check if this assumption makes sense, we refer to figure 13 where we compare the solid-line separating the domains of one and two solutions with two approximated theoretical lines. An approximation for the lower boundary of the solid line can be obtained by a simple equation (dashed line) which states the equality of the drift velocity and the unperturbed phase velocity:

$$\tfrac{1}{2}u_* = c_0. \tag{4.1}$$

Note that (4.1) is motivated by the case of a constant (i.e. a z independent) current. To attain an approximation for the upper boundary, which separates the domains of one and two solutions, we have to consider the fact that the current varies with depth, and compare its vertical decay rate with that of the disturbance. From (2.21), we see that the decay rate of the current is $(2\rho_a u_*)/\mu_w$, whereas the vertical decay rate of the wave is given by k_0; comparing the two yields:

$$\frac{2\rho_a u_*}{\mu_w} = \alpha k_0, \tag{4.2}$$

where α is a somewhat free dimensionless constant. Note that the dash-dot line in figure 13 is plotted with $\alpha = 30$, this value was chosen to obtain a fit at $u_* = 1\,\mathrm{m\,s^{-1}}$.

4.2. *Results for the spatial case*

Similar calculations were made for the spatial case. Computationally, the process of finding the eigenvalues and eigenfunctions is similar to the process previously mentioned. Note that in the spatial, case the eigenvalue problem is nonlinear, since the wavenumber k is the eigenvalue. The iterative search process in this case is more complicated in practice, since the eigenvalue can pass through regions where the solver is not valid during the search; despite this, similar phenomena were detected.

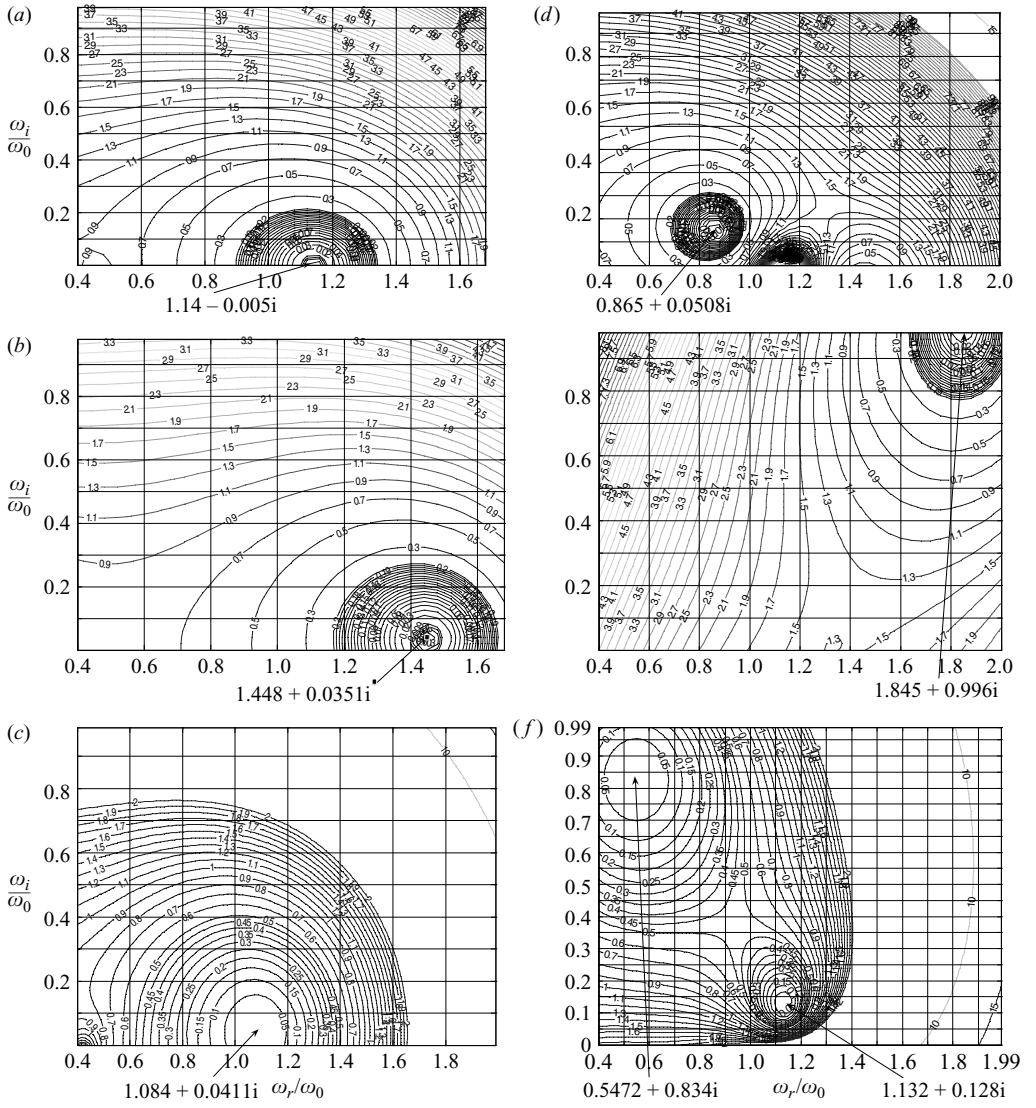

FIGURE 12. Isolines of $\|G\|^2$ for various wind and current conditions and $\lambda = 5\,\mathrm{cm}$. (*a*)- $u_* = 0.3\,\mathrm{m\,s^{-1}}$, no wind, exponential current, the eigenvalue is $\omega/\omega_0 = 1.14 - 0.005\mathrm{i}$, (*b*) $u_* = 0.3\,\mathrm{m\,s^{-1}}$, numeric wind profile, constant current, the eigenvalue is $\omega/\omega_0 = 1.448 + 0.0351\mathrm{i}$, (*c*) $u_* = 0.3\,\mathrm{m\,s^{-1}}$, numeric wind profile, exponential current, the eigenvalue is $\omega/\omega_0 = 1.084 + 0.0411\mathrm{i}$, (*d*) $u_* = 0.8\,\mathrm{m\,s^{-1}}$, no wind, exponential current, the eigenvalue is $\omega/\omega_0 = 0.865 + 0.0508\mathrm{i}$, (*e*)- $u_* = 0.8\,\mathrm{m\,s^{-1}}$, numeric wind profile, constant current, the eigenvalue is $\omega/\omega_0 = 1.845 + 0.996\mathrm{i}$, (*f*)- $u_* = 0.8\,\mathrm{m\,s^{-1}}$, numeric wind profile, exponential current, the eigenvalues are at $\omega/\omega_0 = 0.5472 + 0.834\mathrm{i}$, $\omega/\omega_0 = 1.132 + 0.128\mathrm{i}$. The numeric wind profile is according to the numerical solution of (2.23), and the exponential current is according to (2.21), with $B = 0.5$.

An example for the existence of two unstable modes is presented in figure 14. In figure 14(*a*), the negative sign is due to the harmonic term $\mathrm{e}^{\mathrm{i}(kx-\omega t)}$, hence $-Im(k)$ represents the spatial growth rate. In figure 14(*b*), we show the normalized real wavenumber reciprocal, which is exactly equal to the ratio c/c_0.

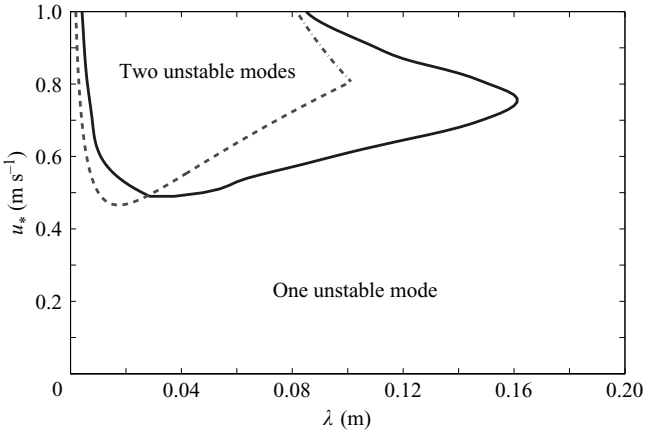

FIGURE 13. Boundary between zones with one and two solutions; numerical computation (solid line), dashed line (4.1) , dash-dotted line (4.2).

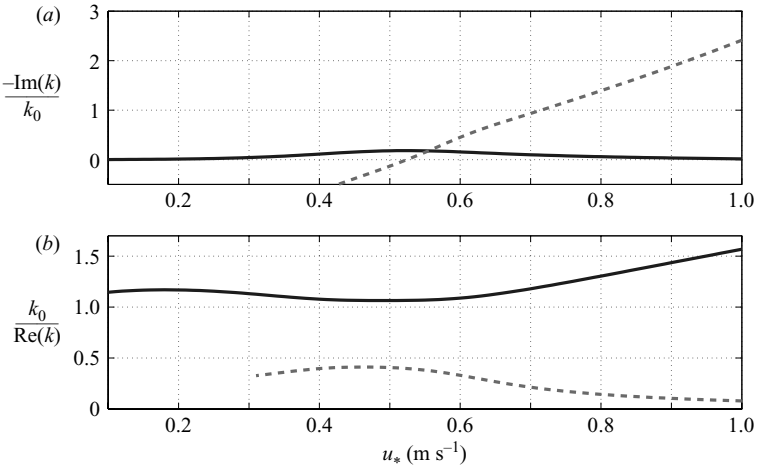

FIGURE 14. Normalized imaginary and real parts of the wavenumber *vs.* friction velocity, two modes are shown in the region of interest, $T = 0.146$ s, ($\lambda_0 = 0.04$ m), spatial case, profile is according to (2.20)–(2.22). (*a*) minus the imaginary part, (*b*)- real part reciprocal.

When comparing figure 14 with figures 6(*a*) and 7(*a*), we can see similar behaviour of these two cases. However, a more detailed investigation is warranted in this case, as well as in the more complicated spatio-temporal case.

4.3. *Is there experimental evidence for the second mode?*

Most of the experimental measurements were mode at relatively weak winds. The only experimental study which conducted measurements at strong winds is Larson & Wright (1974), which measured temporal growth rates under friction velocities up to 1.24 m s^{-1}. If the scenario of two unstable modes is real, we expect that at low wind intensities, as well as at high wind intensities, there should be only one governing mode. For intermediate winds both modes may be relevant. In figure 15, we compare the present results with the experimental results from Larson & Wright (1974), while there are two lines which result from our calculations, there is only one line that

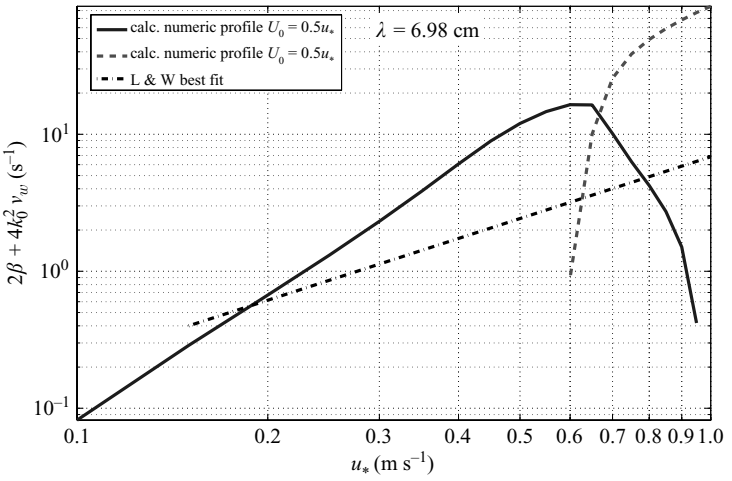

FIGURE 15. Energy growth rate *vs.* friction velocity, comparison with experimental results of Larson & Wright (1974). Profile is according to the numerical solution of (2.23) and (2.21) $B = 0.5$, similar to figure 6(*a*) in Larson & Wright (1974).

approximates the experimental results. As we can see in figure 15, the numerical results and the experimental results do not fit well, the differences are up to a factor of four at the range of $u_* < 0.6\,\mathrm{m\,s^{-1}}$. Despite the poor fit, the evidence that the unstable mode which appears in weak winds decreases and another unstable mode increases while the experimental line increases monotonically, can be taken as support to the very existence of such a second unstable mode. The missing pieces of information in the measurements of Larson & Wright (1974) are the phase velocities and the actual current profile. Information about the phase velocity can be crucial in order to identify the mode, since there are significant differences between the phase velocities of the two modes.

5. Comparison between the viscous and inviscid solutions

5.1. *Comparison for relatively weak winds*

Two questions form the basis of this section. The first deals with the significance of viscosity for such a problem, and the second question is whether Rayleigh's equation are asymptotically (for $Re \to \infty$) an approximation of the Orr–Sommerfeld equations. It is commonly assumed that the inviscid solution is a good approximation of the viscous solution for large Reynolds numbers. The inviscid solution is very practical for many problems, for example, the estimation of lift on an airfoil. In the problem of wave forecasting it is also common to use the inviscid approximation. In wave forecasting, the dominant waves are usually long gravity waves. In our calculation, as already mentioned, we can produce results for the viscous model up to a wavelength of $\lambda = 20\,\mathrm{cm}$. The inviscid solution for the stability problem is very sensitive to the profile and its curvature. The growth rate is proportional to the curvature at the critical point $U_a''(z_{cr})$, where the critical point satisfies $U(z_{cr}) = \mathrm{Re}(c)$. Another important quality of the inviscid solution is that the complex conjugate of a specific eigenvalue is also an eigenvalue. Hence, the inviscid solution predicts no growth for a wind profile with $U''(z_{cr}) = 0$ (linear segment) and none for the case of wave travelling against the wind, where $\mathrm{Re}(c) < 0$ (no critical point). When attempting to compare between the inviscid

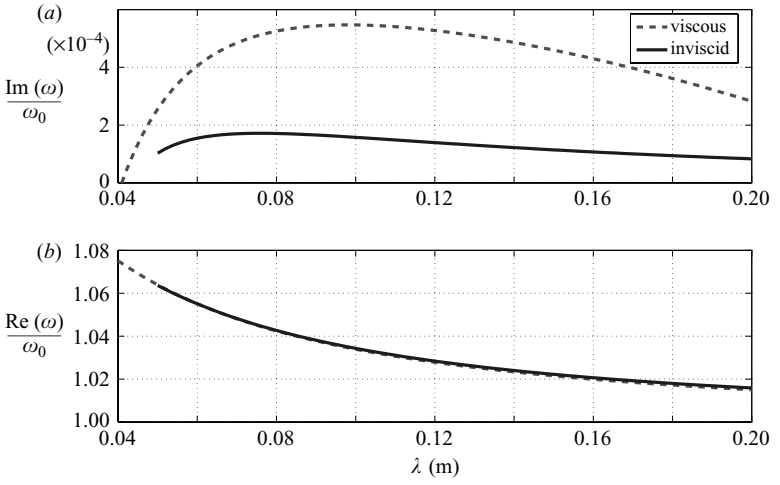

FIGURE 16. Normalized frequency components *vs.* wavelength, for $u_* = 0.06\,\mathrm{m\,s^{-1}}$, comparison between the viscous and inviscid solutions, the profile is according to (2.20)–(2.22). (*a*) Imaginary part, (*b*) real part.

solution and the viscous solution, using the lin–log profile (see (2.20)), we found that the critical point is often inside the linear segment and thus the inviscid model produces no growth. The dashed line in figure 5 is the boundary between the region where the inviscid solution can produce growth and the region where it produces zero growth, for this particular profile. In figure 16, the results of these two models are compared along a cross-section where the inviscid model produces growth. Note that the effect of dissipation due to viscosity does not exist in the inviscid results. The comparison shows very good agreement in the real part of the eigenvalues, which means that they predict waves with almost the same phase velocity. In figure 16(*a*), we can see that the resulting growth rate by these two models is of the same order, but we can state that for most wavelengths the growth predicted by the viscous model is approximately three times larger than that predicted by the inviscid model.

A more detailed comparison tool is to test the dynamic boundary condition plot. The dynamic boundary condition plot is the plot of the isolines of the squared norm of $G(\omega, k)$, see (3.5) and § 3.1. Such a comparison enables us to compare the patterns of these two solutions as well. In figure 17, the dynamic boundary condition plot of these two solutions is presented. As we can see, the pattern of the surface of the solution is almost the same. The arrowhead points to the minimum point of this surface (where $G = 0$), this point is the eigenvalue of the solution. In figure 18, we can see that the structure of the eigenfunctions for the viscous and inviscid solutions is similar in nature, however, the eigenfunctions are somewhat different in their actual values, corresponding to what we have seen in figure 17. Another point which is made clear by figure 18 is the dominance of the critical layer, compared to its insignificance in the case of figure 11. The apparent difference between the two scenarios could be related to the fact that in figure 18 the critical point is in the air and above the laminar viscous layer.

5.2. *Comparison for strong winds*

The comparison between viscous and inviscid solutions using the lin–log profile is limited because of the linear segment which results in zero growth in the inviscid

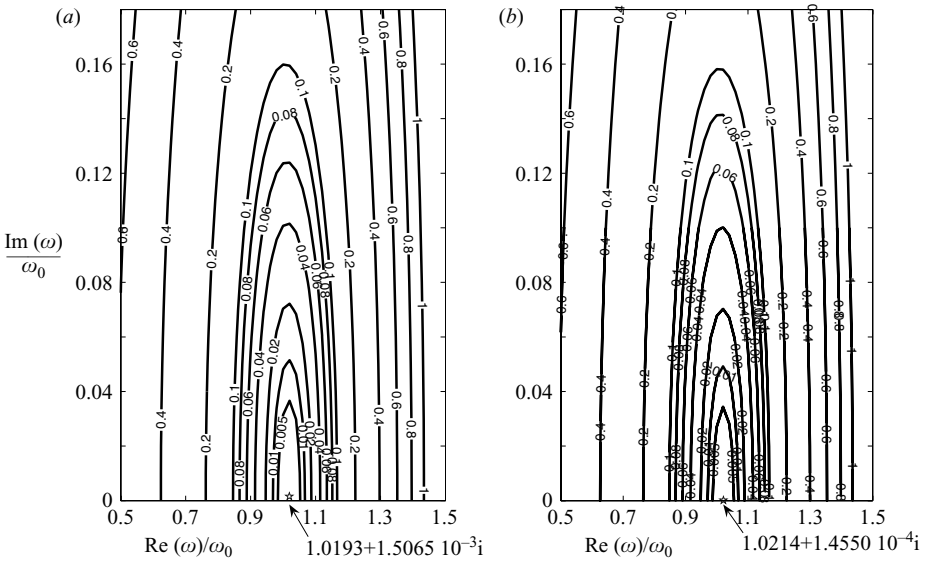

FIGURE 17. Isolines of $\|G\|^2$ in the ω-plane, $u_* = 0.1\,\mathrm{m\,s^{-1}}$, $\lambda = 0.18\,\mathrm{m}$, comparison between viscous and inviscid solutions, profile is according to (2.20)–(2.22). (*a*) Viscous solution, (*b*) inviscid solution.

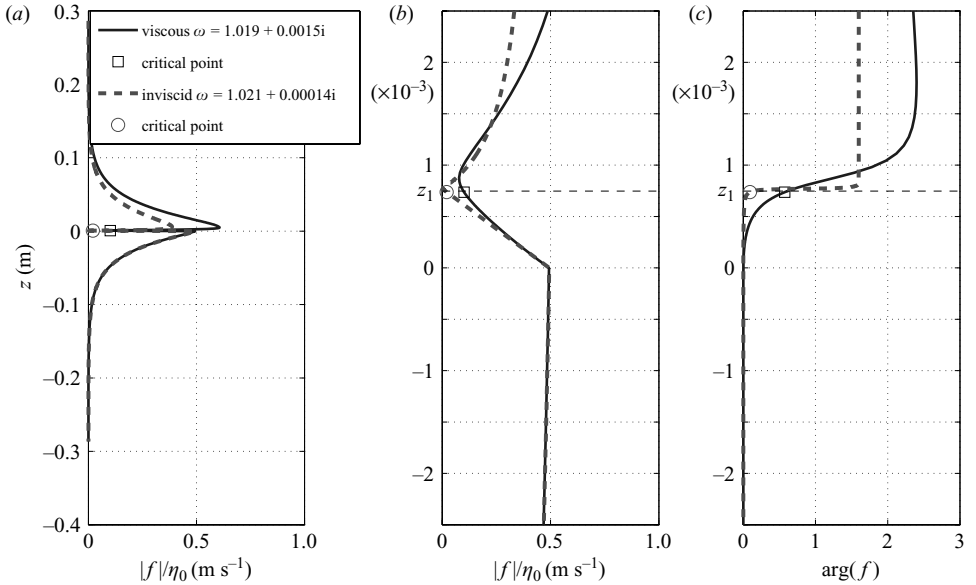

FIGURE 18. Comparison of the eigenfunctions between viscous and inviscid solutions, $u_* = 0.1\,\mathrm{m\,s^{-1}}$, $\lambda = 0.18\,\mathrm{m}$, profile is according to (2.20)–(2.22). (*a*) Absolute value of the eigenfunction, (*b*) absolute value of the eigenfunction, enlargement, (*c*) argument of the eigenfunction, enlargement.

model. In order to compare these two models more comprehensively we looked for a wind profile that is similar to the profile of a turbulent boundary layer and which has non-zero curvature in a layer close to the interface. A good candidate for such a profile is the numerical solution for the mean velocity of the boundary-layer equation,

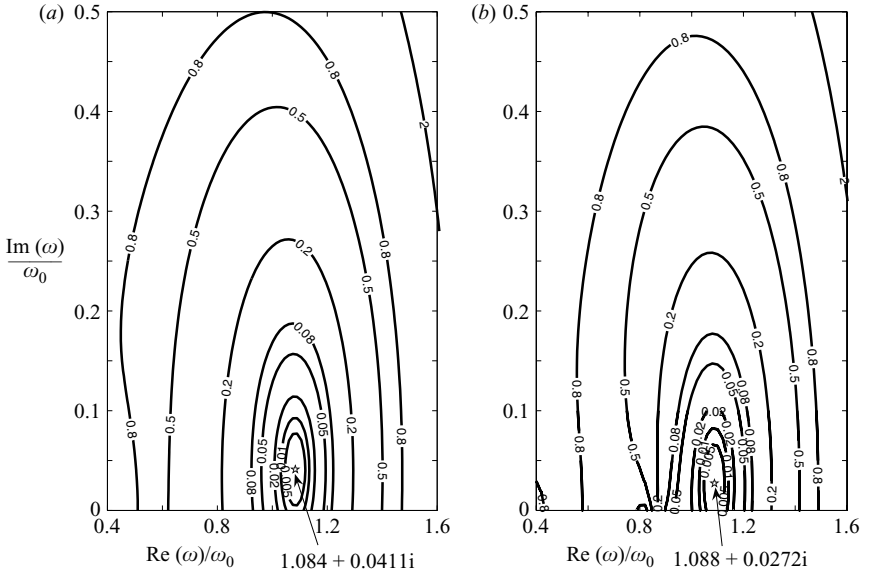

FIGURE 19. Isolines of $\|G\|^2$ in the ω-plane, $u_* = 0.3\,\mathrm{m\,s^{-1}}$, $\lambda = 0.05\,\mathrm{m}$, comparison between viscous and inviscid solutions, profile is according to the numerical solution of (2.23) and (2.21) $B = 0.5$. (*a*) Viscous solution, (*b*) inviscid solution.

which is (2.23). The results of the viscous model, when using this profile with the same exponential current, are very similar to those of the lin–log profile, including the second unstable mode. The use of this profile provides the opportunity to compare between the viscous and inviscid models at stronger winds.

In order to examine the differences between the solutions, we present two comparisons of the dynamic boundary condition plots. In figure 19, the comparison is for $\lambda = 0.05\,\mathrm{m}$, $u_* = 0.3\,\mathrm{m\,s^{-1}}$. As can be seen, the behaviour is similar to figure 17; the real part is almost the same, whereas the imaginary part of the viscous solution is 1.5 times larger than that in the inviscid solution. The pattern of the isolines is very similar.

In figure 20, we present the same comparison, but for a much stronger wind. As can be seen, in this figure the picture is completely different. There is no connection between the solutions, neither in the real part nor in the imaginary part, and even the number of unstable eigenvalues is different.

The comparison at strong winds shows a more dramatic disagreement between the viscous and inviscid models, where not only can the growth rate of the viscous model be a hundred times larger than the growth rate of the inviscid model, but also the real part and the number of unstable modes indicate a disagreement between the models. Within the range of our calculations, the results indicate that the inviscid solution cannot be taken as a sensible approximation to the viscous one.

6. Summary and conclusions

After formulating the linear stability problem of surface waves for a viscous/inviscid fluid, we built a robust solver in order to solve these eigenvalue problems for the spatial and temporal case and a range of mean flow profiles. The results of the solver

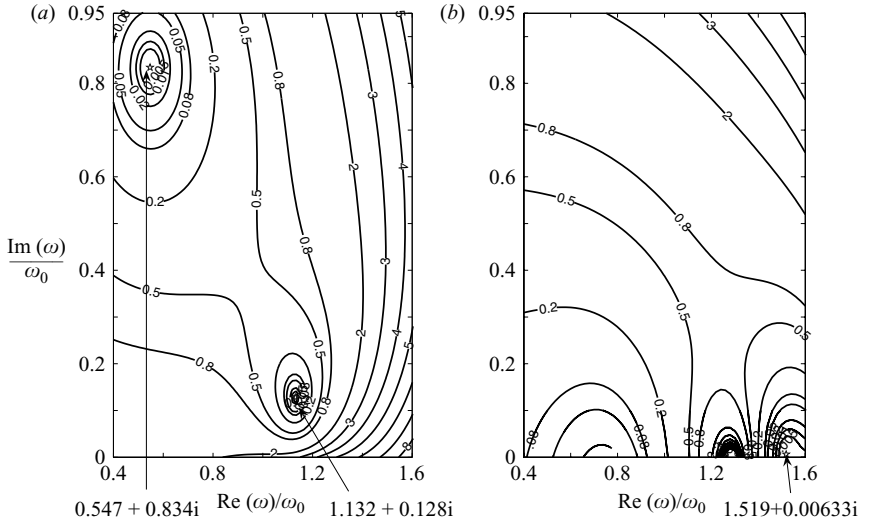

FIGURE 20. Isolines of $\|G\|^2$ in the ω-plane, $u_* = 0.8\,\mathrm{m\,s^{-1}}$, $\lambda = 0.05\mathrm{m}$, comparison between viscous and inviscid solutions, profile is according to the numerical solution of (2.23) and (2.21) $B = 0.5$. (*a*) Viscous solution, (*b*) inviscid solution.

were validated for the range $0 < \lambda < 20\,\mathrm{cm}$, $0 < u_* < 1\,\mathrm{m\,s^{-1}}$, and hence expand the computational domain in the (λ, u_*)-plane, relative to previous studies.

This expansion leads to the discovery of a new unstable mode. The main conditions for the appearance of this mode are the simultaneous existence of a shear flow in the water and a wind intensity above a critical value. A non-vanishing viscosity is also a prerequisite for the appearance of two modes. From the results of the strong wind scenarios, we can say that the nature of the generated waves is significantly different from the nature of waves without the influence of air.

The comparison between the viscous model and the inviscid model at low wind intensities shows very good agreement in the real part of the eigenvalue; however, the comparison of the imaginary part is less agreeable in this case. A comparison for stronger winds shows total disagreement between the two models. All these results lead to the conclusion that the use of the inviscid approximation is problematic at this range of wavelengths, and it will be interesting to see the comparison at wavelengths of the order of $\sim 1\,\mathrm{m}$.

This research is part of an MSc thesis submitted by A. Z. to the Graduate School at the Technion – Israel Institute of Technology. The research was supported by The Israel Science Foundation (Grant 695/04) and by the Fund for Promotion of Research at the Technion.

Appendix. The test case

In this section we present the analytical solution for the case of linear wind profile and constant current. The profile has the form:

$$U_a = U_0 + az, \qquad U_w = U_0. \tag{A 1}$$

The Orr–Sommerfeld equation is:

$$\mathrm{i}\epsilon(f^{(4)} - 2k^2 f'' + k^4 f) + k\left[(U - c)(f'' - k^2 f) - U'' f\right] = 0, \tag{A 2}$$

where $\epsilon_{w,a} = 1/Re_{w,a} = \nu_{w,a}/k_0^2\omega_0$ is the inverse Reynolds number. Substituting (A 1) into (A 2) gives:

$$f^{(4)} - kf''\left(2k + \frac{\mathrm{i}}{\epsilon}(U-c)\right) + k^3 f\left(k + \frac{\mathrm{i}}{\epsilon}(U-c)\right) = 0. \tag{A 3}$$

Now we can define $F \triangleq f'' - k^2 f$. Hence (A 3) becomes:

$$F'' - k\left(k + \frac{\mathrm{i}}{\epsilon}(U-c)\right)F = 0, \tag{A 4}$$

By a transformation of variables, (A 4) is transformed into Airy's equation.

$$F''(u) - uF(u) = 0, \tag{A 5}$$

where:

$$u = \left(\frac{\mathrm{i}\epsilon}{ka}\right)^{2/3} k\left(k + \frac{\mathrm{i}}{\epsilon}(U-c)\right) = \frac{k}{2}(1+\mathrm{i}\sqrt{3})\left(\frac{\epsilon}{ka}\right)^{2/3}\left(k + \frac{\mathrm{i}}{\epsilon}(U-c)\right). \tag{A 6}$$

Thus, $F(u(z))$ is a solution of Airy's equation. Since it is a second-order equation, it has two independent solutions. There are a few common pairs of independent solutions, see Abramowitz & Stegun (1972), Vallee & Soares (2004).

$$\left.\begin{array}{l} \mathrm{Ai}(u),\ \mathrm{Bi}(u) \\ \mathrm{Ai}(u),\ \mathrm{Ai}(u\mathrm{e}^{2\pi i/3}) \\ \mathrm{Ai}(u),\ \mathrm{Ai}(u\mathrm{e}^{-2\pi i/3}) \end{array}\right\} \tag{A 7}$$

Since the solution and its derivative must vanish at infinity, We choose the pair $\mathrm{Ai}(u)$, $\mathrm{Ai}(u\mathrm{e}^{-2\pi\mathrm{i}/3})$, so that:

$$F = f'' - k^2 f = c_1\mathrm{Ai}(u) + c_2\mathrm{Ai}(u\mathrm{e}^{-2\pi\mathrm{i}/3}) \tag{A 8}$$

At this stage, we must look at the asymptotic behaviour of the independent solutions for large values of $|z|$ in order to be sure that we satisfy the boundary condition at infinity. As mentioned in Vallee & Soares (2004), the Airy function Ai blows up for large $|u|$ outside the section $|\arg(u)| < \pi/3$. Hence, we should look at the behaviour of $\arg(u)$ at infinity $z \to \pm\infty$.

$$\arg(u) = \begin{cases} \dfrac{5\pi}{6} + \dfrac{\arg(k)}{3}, & z \to \infty, \\ -\dfrac{\pi}{6} + \dfrac{\arg(k)}{3}, & z \to -\infty, \end{cases} \tag{A 9}$$

$$\arg(u\mathrm{e}^{-2\pi\mathrm{i}/3}) = \begin{cases} \dfrac{\pi}{6} + \dfrac{\arg(k)}{3}, & z \to \infty, \\ -\dfrac{5\pi}{6} + \dfrac{\arg(k)}{3}, & z \to -\infty, \end{cases} \tag{A 10}$$

If we take $Re(k) > 0 \Rightarrow |\arg(k)| < \pi/2$ we can be sure that:

$$|\arg(u)| < \tfrac{\pi}{3}, \qquad z \to -\infty, \tag{A 11}$$

$$|\arg(u\mathrm{e}^{-2\pi i/3})| < \tfrac{\pi}{3}, \qquad z \to \infty, \tag{A 12}$$

Thus in the air:

$$F_a = f_a'' - k^2 f_a = c_1\mathrm{Ai}(u\mathrm{e}^{-2\pi i/3}). \tag{A 13}$$

Solving the above second-order equation:

$$f_a = c_1 \left[\frac{e^{kz}}{2k} \int_0^z e^{-kt} \mathrm{Ai}(ue^{-2\pi i/3}) dt - \frac{e^{-kz}}{2k} \int_0^z e^{kt} \mathrm{Ai}(ue^{-2\pi i/3}) dt \right] + c_2 e^{-kz} + c_3 e^{kz}. \tag{A 14}$$

Since we require decay at infinity:

$$\frac{c_1}{2k} \int_0^\infty e^{-kt} \mathrm{Ai}(ue^{-2\pi i/3}) dt + c_3 \triangleq \frac{c_1}{2k} p_1(k, c, a, U_0) + c_3 = 0, \tag{A 15}$$

$$c_3 = -\frac{c_1}{2k} p_1. \tag{A 16}$$

For the case of constant current in the water $U_w \equiv U_0$, the solution for the water will be:

$$f_w = b_1 \exp(kz) + b_2 \exp(\pm \sqrt{k \left(k + \frac{i}{\epsilon}(U_0 - c) \right)} z) \triangleq b_1 \exp(kz) + b_2 \exp(Bz). \tag{A 17}$$

If $Re(B) < 0$, we must choose e^{-Bz} as the second independent solution; and if $Re(k) < 0$, we must choose e^{-kz} instead of e^{kz}.
And the derivatives are:

$$f_w' = k b_1 e^{kz} + B b_2 e^{Bz}, \tag{A 18}$$

$$f_w'' = k^2 b_1 e^{kz} + B^2 b_2 e^{Bz}, \tag{A 19}$$

$$f_w''' = k^3 b_1 e^{kz} + B^3 b_2 e^{Bz}. \tag{A 20}$$

At the interface it reduces to:

$$\left. \begin{array}{ll} f_w(0) = b_1 + b_2, & f_w'(0) = k b_1 + B b_2, \\ f_w''(0) = k^2 b_1 + B^2 b_2, & f_w'''(0) = k^3 b_1 + B^3 b_2. \end{array} \right\} \tag{A 21}$$

In order to find the unknown coefficients, we must apply the boundary conditions at the interface. In these boundary conditions the derivatives of f play a main role. Thus, we must calculate $f_{w,a}(0)$, $f_{w,a}'(0)$, $f_{w,a}''(0)$, $f_{w,a}'''(0)$. This must be done carefully, using Leibniz's rule for differentiation of integrals.

$$\frac{d}{dz} \int_{f_1(z)}^{f_2(z)} g(t) dt = g(f_2(z)) f_2'(z) - g(f_1(z)) f_1'(z). \tag{A 22}$$

Hence:

$$f_a' = c_1 \left[\frac{e^{kz}}{2} \int_0^z e^{-kt} \mathrm{Ai}(ue^{-2\pi i/3}) dt + \frac{e^{-kz}}{2} \int_0^z e^{kt} \mathrm{Ai}(ue^{-2\pi i/3}) dt \right] - k c_2 e^{-kz} + k c_3 e^{kz}, \tag{A 23}$$

$$f_a'' = c_1 \left[\frac{k e^{kz}}{2} \int_0^z e^{-kt} \mathrm{Ai}(ue^{-2\pi i/3}) dt - \frac{k e^{-kz}}{2} \int_0^z e^{kt} \mathrm{Ai}(ue^{-2\pi i/3}) dt + \mathrm{Ai}(ue^{-2\pi i/3}) \right] + k^2 c_2 e^{-kz} + k^2 c_3 e^{kz} \tag{A 24}$$

$$f_a''' = c_1 \left[\frac{k^2 e^{kz}}{2} \int_0^z e^{-kt} \mathrm{Ai}(ue^{-2\pi i/3}) dt + \frac{k^2 e^{-kz}}{2} \int_0^z e^{kt} \mathrm{Ai}(ue^{-2\pi i/3}) dt + \mathrm{Ai}'(ue^{-2\pi i/3}) e^{\pi i/6} \left(\frac{ka}{\epsilon} \right)^{1/3} \right] - k^3 c_2 e^{-kz} + k^3 c_3 e^{kz} \tag{A 25}$$

It will be helpful to use the following notation:

$$u(0) = u_0 = \left(\frac{\mathrm{i}\epsilon}{ka}\right)^{2/3} k\left(k + \frac{\mathrm{i}}{\epsilon}(U_0 - c)\right), \tag{A 26}$$

$$\mathrm{Ai}(u(0)\mathrm{e}^{-2\pi\mathrm{i}/3}) = \tilde{\mathrm{A}}\mathrm{i}_0 = \mathrm{Ai}(u_0\mathrm{e}^{-2\pi\mathrm{i}/3}), \tag{A 27}$$

$$\mathrm{Ai}(u(0)) = \mathrm{Ai}_0 = \mathrm{Ai}(u_0). \tag{A 28}$$

Now we can present the derivatives at the interface:

$$\left.\begin{gathered} f_a(0) = c_2 + c_3, \quad f_a'(0) = k(c_3 - c_2), \quad f_a''(0) = c_1\tilde{\mathrm{A}}\mathrm{i}_0 + k^2(c_2 + c_3), \\ f_a'''(0) = c_1\tilde{\mathrm{A}}\mathrm{i}_0'\mathrm{e}^{\pi\mathrm{i}/6}\left(\tfrac{ka}{\epsilon}\right)^{1/3} + k^3(c_3 - c_2), \end{gathered}\right\} \tag{A 29}$$

$$\left.\begin{gathered} f_w(0) = b_1 + b_2, \qquad f_w'(0) = kb_1 + Bb_2, \\ f_w''(0) = k^2 b_1 + B^2 b_2, \qquad f_w'''(0) = k^3 b_1 + B^3 b_2. \end{gathered}\right\} \tag{A 30}$$

Writing the boundary condition at the interface:

$$f_a(0) = f_w(0) = c - U_0 \Rightarrow c_2 + c_3 = b_1 + b_2 = c - U_0, \tag{A 31}$$

$$f_w'(0) + U_w'(0) = f_a'(0) + U_a'(0) \Rightarrow k(c_3 - c_2) = kb_1 + Bb_2 - a_a, \tag{A 32}$$

$$\begin{gathered} \mu(f_a''(0) + k^2 f_a(0) + U_a''(0)) = (f_w''(0) + k^2 f_w(0) + U_w''(0)) \\ \Rightarrow \mu(c_1\tilde{\mathrm{A}}\mathrm{i}_0 + k^2(c_2 + c_3) + k^2(c_2 + c_3)) = k^2 b_1 + B^2 b_2 + k^2(b_1 + b_2) \\ \Rightarrow \mu c_1\tilde{\mathrm{A}}\mathrm{i}_0 - k^2 b_1 - B^2 b_2 = k^2(c - U_0)(1 - 2\mu). \end{gathered} \tag{A 33}$$

We obtain a system of five linear equations with five unknowns c_1, c_2, c_3, b_1, b_2. After solving the system we have the value of the functions f_a, f_w and their derivatives at the interface. Note that all of these constants are functions of the specific case which is defined by (R_a, R_w, a, U_0) and the value of ω, k. After we obtain these values, we can substitute them into the dynamic boundary condition and solve it, in order to find ω, k.

$$\begin{aligned} &kf_w'(c - U_0) + kf_w U_w' + \mathrm{i}R_w^{-1}(3k^2 f_w' - f_w''') - F \\ &\quad = \rho\left[kf_a'(c - U_0) + kf_a U_a' + \mathrm{i}R_a^{-1}(3k^2 f_a' - f_a''') - F\right] + Wk^3 \ \textit{at}\ z = 0 \end{aligned} \tag{A 34}$$

In practice, we are unable to obtain a simple dispersion relation for this case, thus in order to calculate it we must do it numerically. The value of the constant p_1 (see equation (A 15)) can be calculated numerically and then the dispersion equation will be solved by a numeric solver for a nonlinear equation.

REFERENCES

Abramowitz, M. & Stegun, I. A. 1972 *Handbook of Mathematical Functions*. Dover.

Boomkamp, P. A. M., Boersma, B. J., Miesen, R. H. M. & Beijnon, G. V. 1997 Chebyshev collocation method for solving two-phase flow stability problem. *J. Comput. Phys.* **132**, 191–200.

Caulliez, G., Ricci, N. & Dupont, R. 1998 The generation of the first visible wind waves. *Phys. Fluids Lett.* **10**, 757–759.

Charnock, H. 1955 Wind stress on water surface. *Q. J. R. Met. Soc.* **81**, 639–640.

Jeffreys, H. 1925 On the formation of water waves by wind. *Proc. R. Soc.* A **104**, 189–206.

Kawai, S. 1979 Generation of initial wavelets by instability of a coupled shear flow and their evolution to wind waves. *J. Fluid Mech* **93**, 661–703.

Larson, T. R. & Wright, J. W. 1974 Wind-generated gravity capillary waves: laboratory measurements of temporal growth rates using microwave backscatter. *J. Fluid Mech.* **70**, 417–436.

Miles, J. W. 1957*a* On the generation of surface waves by shear flows. *J. Fluid Mech.* **3**, 185–204.

Miles, J. W. 1957*b* On the velocity profile for turbulent flow near a smooth wall. *J. Aero. Sci.* **24**, 704.

Phillips, O. M. 1957 On the generation of waves by turbulent wind. *J. Fluid Mech.* **2**, 417–445.

Powell, M. D., Vickery, P. J. & Rienhold, T. A. 2003 Reduced drag coefficient for high wind speeds in tropical cyclones. *Nature* **422**, 279–283.

Stiassnie, M., Agnon, Y. & Janssen, P. A. E. M. 2007 Temporal and spatial growth of wind waves. *J. Phys. Oceanogr.* **37**, 106–114.

Trefethen, L. N. 2000 *Spectral Methods in MATLAB*. SIAM.

Tsai, W. T. & Lin, M. Y. 2004 Stability analysis on the initial surface-wave generation within an air-sea coupled shear flow. *J. Mar. Sci. Technol.* **12**, 200–208.

Tsai, Y. S., Grass, A. J. & Simons, R. R. 2005 On the spatial linear growth of gravity–capillary water waves sheared by a laminar air flow. *Phys. Fluids* **17**, 095101–1–095101–13.

Valenzuela, G. R. 1976 The growth of gravity-capillary waves in a coupled shear flow. *J. Fluid Mech.* **76**, 229–250.

Vallee, O. & Soares, M. 2004 *Airy Functions and Application to Physics*. Imperial College Press.

Van Gastel, K., Janssen, P. A. E. M. & Komen, G. J. 1985 On phase velocity and growth rate of wind-induced gravity-capillary waves. *J. Fluid Mech.* **161**, 199–216.

Wheless, G. H. & Csanady, G. T. 1993 Instability waves on the air–sea interface. *J. Fluid Mech.* **248**, 363–381.

Zhang, X. 2005 Short surface waves on surface shear. *J. Fluid Mech.* **541**, 345–370.

Zhang, X. & Harrison, S. 2004 A laboratory observation of the surface temperature and velocity distributions on a wavy and windy airwater interface. *Phys. Fluids* **16**(1), L5–L8.